Optimizing free parameters in the D3Q19 Multiple-Relaxation lattice Boltzmann methods to simulate under-resolved turbulent flows

M. Chávez-Modena[a,b], A. Martínez-Cava[a,b], G. Rubio[a,b] and E. Ferrer[a,b]

[a] *ETSIAE - Universidad Politécnica de Madrid - Plaza de Cardenal Cisneros 3, 28040 Madrid, Spain*

[b] *Center for Computational Simulation - Universidad Politécnica de Madrid, Campus de Montegancedo, Boadilla del Monte, 28660 Madrid, Spain*
m.chavez@upm.es

Abstract

We present a D3Q19 lattice scheme based in MRT with central moments (MRT-CM), where the free parameters of the model are optimized to dissipate under-resolved flow structures with high wavenumbers. In Chávez-Modena et al. in Computers & Fluids 172:397-409, 2018 [1], we compared the BGK, MRT-RM and MRT-CM for the D2Q9 lattice scheme using von Neumann analyses and quantified their numerical properties. Based on this study, we proposed an optimized 2D MRT-CM scheme with enhanced stability for under-resolved flows. Here, we extend this idea to the D3Q19 MRT-CM scheme.

As before, we base our optimization for the free parameters, on the k-1% dispersion-error rule, that states that waves with dispersive errors above 1% should be dissipated since they pollute the solution and may cause instabilities. To this aim we increase dissipation in the scheme for waves with dispersive errors above 1%.

The resulting optimized scheme is verified through a von Newmann analysis and validated for the three-dimensional Taylor-Green isotropic turbulent flow. We show how the original D3Q19 MRT-CM (d'Humières version) leads to unrealistic kinetic energy accumulation at high wave numbers, whilst our optimized MRT-CM provides the correct energy dissipated rate, avoiding energy build up

at high wavenumbers. These results suggest that our optimization strategy enhances stability and allows for accurate energy spectra in under-resolved flow simulations such as typically found in Large Eddy Simulations.

Keywords: Lattice Boltzmann, D3Q19 multiple-relaxation time, rule of k-1% dispersion-error, homogeneous isotropic turbulence.

---

1. Introduction

Over the last decades, the Lattice Boltzmann method (LBM) has become an alternative to traditional discretization techniques of the Navier-Stokes (NS) equations to simulate fluid flows. Thanks to the efficient parallelization [2], the LBM has a high computing performance being competitive against NS approaches for many applications [3, 4], in particular for the simulation of turbulent flows [5, 6]. The LBM is capable of simulating situations where sound and flow interact, such as aeroacoustic generation [7, 8]. Additionally, it is used to simulate a wide range of multiphase [9, 10] and multicomponent [11] flows.

The collision operator is responsible of modeling the physics correctly, and has a strong effect in the numerical stability of the scheme [12, 13]. Several collision operators have been proposed to extend the range of applicability of the LBM. Recently, Coreixas et al. [14] proposed a formalism that encompasses all these approaches within a common mathematical framework. In this work, we focus into the single BGK and multiple-relaxation MRT time collision operators.

The most popular collision operator, the single-relaxation time, is based on the BGK [15] approximation. In this model a unique relaxation time is considered for all the probability distribution functions. As a result of its simplicity, it has severe stability limitations [16], precluding its use at low viscosities, large Mach numbers or under-resolved simulations.

The multiple-relaxation time with raw moments (MRT-RM) collision operator [17] was introduced in an attempt to improve the BGK stability limitations. This operator enables different relaxation times for each probability distribution

function. The increased complexity with respect to BGK resulted in an improved numerical stability [18].

Despite the enhancement in the stability of the MRT-RM with respect to the BGK collision operator, the MRT-RM can still show instabilities for small fluid viscosities [19]. Consequently, the MRT with central moments (MRT-CM) collision operator was introduced [20]. Premnath and Banerjee [21] showed that the cascaded LBM with central moments is consistent with the Navier-Stokes equations via a Chapman-Enskog expansion, and that in this approach, Galilean invariance is naturally enforced based on the relaxation central moments, see also [22]. Using central moments for the collision operator, it is possible to enhance the numerical stability by increasing the numerical dissipation at high wavenumbers [1].

Von Neumann stability analyses [23] enable the quantification of numerical errors in numerical schemes with periodic boundary conditions. Sterling and Chen [24] were the first to apply this analysis to the LB BGK approach. Then, Lallemand and Luo [18] used it to compare the enhanced stability of the MRT-RM over the BGK approach. Subsequently, Siebert et al. [25] included high order terms into the equilibrium distribution of the D2Q9 model to improve the linear stability of the scheme (as shown depicted Fig. 2 in [25]). Malaspinas [26] proposed a new version of the BGK with improved stability and based on recursive relations and regularization for the LB posed as Hermite series, which has been subsequently validated by Mattila et al. [27] and Coreixas et al. [28]. Later, in our previous work [1], we showed how the MRT-CM is more dissipative at higher wavenumbers compared with BGK and MRT-RM, providing better numerical stability. Also, we explored higher order terms in the fluid velocity, following Malaspinas' work [26] to observe that our proposed approach provides similar results, with comparable stability, and for similar range of Mach numbers.

In addition to quantifying the numerical stability, this technique can also be used to provide insights into dispersive and dissipative errors. Marié et al. [29] compared BGK and MRT-RM collision operators. Dubois et al. [30] studied

the numerical stability of the relative velocity (MRT-RM and MRT-CM) D2Q9 schemes with two different set of moments, proposed by Lallemand and Luo [18] and Geier et al. [19]. They concluded that MRT-CM with Geier's moment basis [19] had better stability properties. Recently, Gauthier et al. analyzed the interaction between modes [31] to understand the reason of numerical instabilities.

As mentioned, both the MRT-RM and the MRT-CM relax each hydrodynamic moment with a different relaxation time but all combinations lead to the same macroscopic state through the Chapman-Enskog expansion [32]. The relaxation times that are not fixed by the physics of interest become free parameters that can be optimized to enhance particular numerical aspects. Lallemand and Luo [18] optimized these parameters (for the D2Q9 lattice scheme) maximizing the Galilean invariance of the scheme, while reducing numerical errors (i.e. dispersion and dissipation). Similarly, Xu and Sagaut [7, 33] proposed an optimization to minimize dispersion/dissipation errors for the MRT-RM in D2Q9 scheme. A different approach is to adjust the high order relaxation parameters to enhance the stability for under resolved simulations. This approach was used by Ning et al. [34] to improve the stability of a 2D central moment LB method for a lid driven cavity flow problem. However, the authors of that work stated that their results were problem-dependent, and that additional work was required in 3D to optimize the relaxation parameters of the cascaded MRT LBM by means of a Fourier linear analysis. Adam et al. [22] proposed a cascaded LBM for the D3Q19 in the context of non-Newtonian flows. In their approach the free parameter were set to 1 (i.e., equilibrium), although it was already noticed that these could be adjusted independently to improve numerical stability by means of a Fourier linear stability analysis. These ideas were recently exploited by the authors [1], where the D2Q9 MRT-CM scheme was optimized to increase dissipation only for high under-resolved wavenumbers (above the k-1% dispersion-error), leaving low wavenumbers (i.e. well resolved scales) unchanged. This was tested successfully in the double periodic shear layer test.

In this work we extend our previous work to improve the MRT-CM for three-

dimensional flows. The optimization strategy used previously for the D2Q9 lattice scheme [1] is now extended to the D3Q19 scheme. Again, instead of minimizing dissipation errors for all wavenumbers, we propose to maintain numerical dissipation for well resolved wavenumbers whilst increasing dissipation for under-resolved wavenumbers. The optimization is inspired in the rule of k-1% dispersion-error presented by Moura et al. [35] in the context of high order numerical methods. They suggested that waves are only accurately resolved if the dispersion error (difference between theoretical and numerical) is below 1%. The wavenumber at which the error becomes 1% was named "k-1% dispersion-error" and lead to the "1% rule". Following this rule, all waves above the k-1% should be dissipated since these are poorly resolved and may pollute the solution. We follow the idea of damping under-resolved waves and apply it to the LBM for the first time in a 3D lattice scheme.

To assess the D3Q19 optimized MRT-CM, we simulate the Taylor-Green vortex (TGV) case [36] that includes starting transitional flow followed by decaying homogeneous turbulence. This case enables the quantification of vortex stretching/pairing processes leading to energy cascading from large to small eddies, allowing the study of the dynamics of transition from laminar to turbulent flow and subsequent turbulent energy decay. This test-case has been widely used to study dissipation errors of numerical schemes, of high order type, e.g. [37, 38] and for LB schemes, e.g. [39, 40, 41].

The remaining of this text is organized as follows. First, in Section 2, we describe the numerical methodology which is divided in two parts: first, the Lattice Boltzmann method with the different collision operators and second the optimization strategy. Then, in Section 3, the results of the optimized approach are tested for the turbulent Taylor Green Vortex case. Finally, in Section 4 conclusions are presented.

2. Methodology

In this section the numerical methodology used in this work is presented. First, the Lattice Boltzmann method (LBM) is introduced. Special attention is paid to the definition of the collision operator. Secondly, an optimization method based on linear stability analysis is shown. The optimization aims at maximizing the robustness of the scheme for under-resolver simulations without penalizing its accuracy. The final objective is to improve the performance of the scheme for turbulent flows, therefore a three dimensional LBM scheme, in particular the D3Q19, is considered.

2.1. Lattice Boltzmann method

2.1.1. Generalities

The LBM is a numerical technique that provides numerical solutions of the continuous Boltzmann equation. The discrete Boltzmann equation reads:

$$f_i(\mathbf{x} + \mathbf{e}_i \Delta t, t + \Delta t) - f_i(\mathbf{x}, t) = \Delta t \Omega_i(\mathbf{x}, t),\ i = 0, ..., Q - 1. \tag{1}$$

The discrete set of velocities is a vector of Q components represented by the symbol $\mathbf{e}_i$. As a consequence, the discrete probability distribution functions (PDFs), $f_i(\mathbf{x}, \mathbf{e}_i, t)$, are stored at each lattice node for each time step, Δt. At each time step, the information stored in the discrete PDFs is streamed through the lattice and collided. The discrete collision operator, Ω_i, is responsible of computing the post-collision state conserving mass and linear momentum.

The collision operator is of critical importance in the LBM, as it is responsible of the modelization of the physics. The first approach for the collision operator was proposed by McNamara [42], but it was still rather complicated. The high cost of its evaluation precluded its use until Higuera and Jimenez [13] simplified this operator by performing linearization (under the assumption that the discrete PDF, f_i, is close to its equilibrium state). Expanding the discrete collision operator, Ω_i, around the equilibrium state of the discrete PDF, f_i^{eq}, leads to

a linearized operator:

$$\Omega_j = K_{ji}(f_i^{\mathrm{eq}} - f_i), \tag{2}$$

where K_{ji} is known as collision matrix, and was further simplified to obtain the different collision operators. The collision matrix describes how the PDFs relax towards the equilibrium state. It is directly related with the viscosity and Mach number.

The discrete local equilibrium function f_i^{eq} is usually computed as a second order Taylor expansion of the Maxwell-Boltzmann distribution,

$$f_i^{\mathrm{eq}} = \rho w_i \left(1 + \frac{\mathbf{e_i}\cdot\mathbf{u}}{c_s^2} + \frac{(\mathbf{e_i}\cdot\mathbf{u})^2}{2c_s^4} - \frac{\mathbf{u}\cdot\mathbf{u}}{2c_s^2}\right), \tag{3}$$

where w_i are weighting constants built to preserve isotropy and c_s is the speed of sound. The particular values of the weighting constants w_i, depend on the discrete set of velocities [43].

2.1.2. Collision operators

Single-relaxation time

The single-relaxation time based on the Bhatnagar-Gross-Krook (BGK) [15] approximation is the most popular approach for the collision operator. In this case, using $K_{ji}^{\mathrm{BGK}} = (1/\tau)\delta_{ij}$ (assuming δ_{ij} *Kronecker* delta notation) the collision operator simplifies to:

$$\Omega_i^{\mathrm{BGK}} = \frac{1}{\tau}(f_i^{\mathrm{eq}} - f_i). \tag{4}$$

Only one relaxation time for all PDFs, τ, is considered. The Chapman-Enskog expansion applied to the classical LBM equation (Eq. 1), with Eq. 4 as the discrete collision operator, establishes the relation between the relaxation time, the kinematic shear, ν, and bulk viscosities, η, of the macroscopic fluid [44]:

$$\nu = c_s^2(\tau - \frac{\Delta t}{2}), \quad \eta = \frac{2}{D}\nu, \tag{5}$$

where D is the dimension space. The BGK collision operator, is still widely used but has several shortcomings. For example, the kinematic viscosity is conditioned by the relaxation parameter, τ, (see Eq. 5) which causes numerical instabilities for values near $\tau = 0.5$ (with $\Delta t = 1$), therefore complicating the simulation of high Reynolds number flows [16]. It should also be noticed that the bulk viscosity, η, cannot be freely chosen because it is constrained by the kinematic viscosity, ν.

Multiple-relaxation time

In the MRT, the relaxation matrix is computed as a product of three matrices, $K_{ji}^{\mathrm{MRT}} = M_{jk}^{-1} S_{kl} M_{li}$. The matrix M accounts for the definition of the moments while the matrix S is defined as a diagonal matrix:

$$S_{kl} = s_k \delta_{kl}, \tag{6}$$

where $\mathbf{s}$ is a vector with relaxation times for the different moments. The MRT-CM collision operator is obtained defining the collision matrix as $K_{ji}^{\mathrm{MRT-CM}} = M_{jk}(\mathbf{u})^{-1} S_{kl} M_{li}(\mathbf{u})$:

$$\Omega_j^{\mathrm{MRT-CM}} = M_{jk}(\mathbf{u})^{-1} S_{kl} M_{li}(\mathbf{u})(f_i^{\mathrm{eq}} - f_i). \tag{7}$$

This notation, first presented by Dubois et al. [45], proposes a more general formulation than Geier's [19], which allows working with the equilibrium PDF, f_i^{eq} defined in the BGK model. Under this framework, taking $\mathbf{u} = 0$, one recovers the MRT with raw moments (MRT-RM) presented by d'Humières [17], whilst setting $\mathbf{u}$ as the fluid velocity provides Geier's method. Let us note that Dubois et al. formulation is equivalent to Geier's (for $\mathbf{u}$ set to the fluid velocity) but the latter uses equilibrium distributions directly derived from the Maxwellian distributions, unlike the former who considered arbitrary velocity fields. Additionally, note that the BGK collision operator can be recovered by setting all the diagonal elements S_{ii} to $1/\tau$.

The formulation introduced up to this point is general for any lattice distribution and spatial dimensions. In this work we aim at improving the performance of LBM for under-resolved turbulent flows, therefore a three dimensional LBM is considered. In particular we focus on the popular D3Q19, whose moment matrix, M, can be found in Appendix A.

2.2. Optimization method for the MRT-CM

In this section the optimization method to improve the performance of LBM for turbulent flows is introduced. This method, proposed by the authors in a previous work [1], modifies the relaxation times of the collision operator in order to maximize the dissipation of under-resolved wavelengths. The optimization method makes use of linear stability analysis to separate well-resolved and under-resolved wavelengths.

2.2.1. Linear stability analysis

Theoretical modes

The theoretical modes are obtained through an analytic linearization of the NS equations [46]. The resulting hydrodynamic modes are known as shear mode, ω_t^s, and acoustic modes, $\omega_t^{\pm}$. The first is related to the kinematic shear viscosity. The second is related to both kinematic shear and bulk viscosities. The analytical expressions for the theoretical hydrodynamic modes read:

$$\begin{aligned} \omega_t^s &= \mathbf{u}\cdot\mathbf{k} - \mathrm{i}\nu|\mathbf{k}|^2, \\ \omega_t^{\pm} &= (\mathbf{u}\pm c_s)\cdot\mathbf{k} - \mathrm{i}[\tfrac{(D-1)}{D}\nu + \frac{\eta}{2}], \end{aligned} \tag{8}$$

where $\mathbf{k}$ is the wavenumber. For an illustrative purpose Figure 1 depicts dispersion (real part of ω, Re(ω)) and dissipation (imaginary part of ω, Im(ω)) behavior for a range of wavenumbers $[0,\pi]$, following Eq. 8 for three-dimensions (D=3), $\mathbf{u}=\{u_x,0,0\}$ and $\mathbf{k}=\{k_x,0,0\}$.

Numerical modes

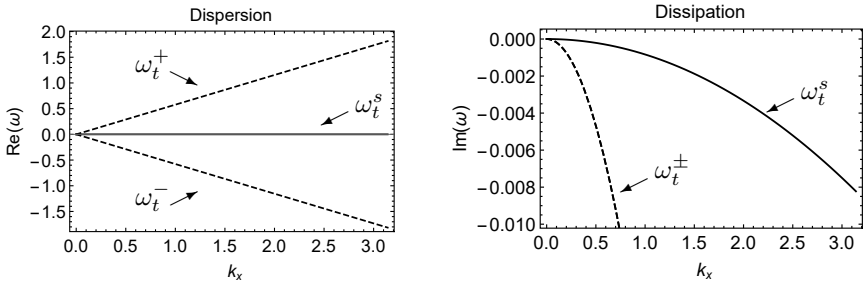

(a) (b)

Figure 1: Dispersion, Re(ω), (a) and dissipation, Im(ω), (b) of the three-dimension theoretical shear mode, ω_t^s: ▬, and acoustic modes, $\omega_t^\pm$: ▪▪, at Ma $= 0$ with $\nu = 10^{-3}\frac{m^2}{s}$ and $\eta = 3.66 \cdot 10^{-2}\frac{m^2}{s}$.

The numerical modes can be obtained by means of von Neumann (VN) analysis [24]. Von Neumann analysis splits the PDF into an equilibrium state, $\bar{f}_i$, plus a perturbation, $\delta f_i(x,t)$:

$$f_i(x,t) = \bar{f}_i + \delta f_i(\mathbf{x},t). \tag{9}$$

The first term in the right hand side, $\bar{f}_i$, is the global PDF, which does not vary with time and space i.e., it depends only on the average density and velocity. The second term in the right hand side, $\delta f_i(x,t)$, accounts for the fluctuations from equilibrium. The fluctuation is assumed as a sinusoidal wave $F_i e^{i(\mathbf{kx}-\omega t)}$ with an amplitude F_i.

Substituting Eq. 9 into Eq. 2, expanding the f_i^{eq} by means of Taylor series centred at the global distribution and after rearranging the expression, an eigenvalue problem is obtained, $F_i\lambda = F_j G_{ij}$, where $\lambda = e^{-i\omega\Delta t}$ are the eigenvalues of the amplification matrix, G_{ij}, defined as:

$$G_{ij} = A_{ik}^{-1}\left[\delta_{kj} + \Delta t K_{kn} N_{nj}\right] \text{ with } \begin{cases} A_{ik} = \delta_{ik} e^{i\mathbf{k}\Delta t \mathbf{e_i}}, \\ N_{nj} = \frac{\partial f_n^{eq}}{\partial f_j} - \delta_{nj}, \end{cases} \tag{10}$$

where the different collision matrices, K_{ij}, are defined in Section 2.1.2. For more details on the VN analysis for the LBM, see [24, 1].

2.2.2. Optimization process: Rule of k-1% dispersion-error

The optimization described here has been inspired by the rule of k-1% dispersion-error proposed by Moura et al. [35] in the context of hp-spectral methods [47, 48, 38]. Moura et al. suggested that wavenumbers with dispersion errors (difference between theoretical and numerical dispersion modes) higher than 1% should be dissipated, since high dispersion errors tend to pollute the solution. In other words, a high dissipative error at high wavenumbers is a positive feature of a numerical method. In a previous work [1], we proposed to optimize the values of the free relaxation times (those affecting moments of order higher than two), to maximize the dissipation of the shear mode in wavenumbers higher than the k-1% dispersion-error wavenumber for the D2Q9 MRT-CM. The dissipation level is measured as the area defined by the theoretical shear mode and numerical shear mode curves for wavenumbers higher than k-1% dispersion-error wavenumber (green area in Figure 2). The error for the k-1% dispersion-error is calculated with the shear mode (theoretical and numerical) by means of the following expression:

$$\%Error(\mathbf{k}) = \frac{|\omega_s - \omega_s^t|}{\omega_s^t} \cdot 100. \tag{11}$$

As the rule describes, k-1% dispersion-error wavenumber occurs when this error is 1%. The dissipation of acoustic modes has not been taken into account because they barely change with the free parameters.

2.2.3. Optimized MRT-CM

This section details the optimization process for D3Q19 MRT-CM lattice scheme. The optimization aims at maximizing the dissipation of the shear mode in wavenumbers higher than the k-1% dispersion-error wavenumber by modifying the values of the free relaxation times (s_{10-18}).

The free parameters $s_{10,11,12}$, $s_{13,14,15}$ and $s_{16,17,18}$ are grouped due to symmetries of the moment constraints. Only the first two groups are considered in the optimization since, as shown later in this section, the last group does not

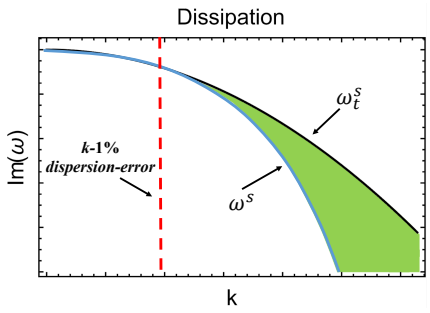

Figure 2: Dissipation area calculated from the difference between the theoretical, ω_s^t,and numerical, ω_s,shear mode.

affect the shear dissipation mode. As a result, $s_{16,17,18}$ has been fixed to 1.4, the value proposed by d'Humières [49]. The flow direction and the perturbations are considered parallel to the lattice direction in the optimization process, i.e., $\mathbf{u} = \{u_x, 0, 0\}$ and $\mathbf{k} = \{k_x, 0, 0\}$. As numerical and theoretical modes depend on the fluid conditions (Mach number, Ma and viscosity ν), the free relaxation times of the model have been optimized for different values of Mach number (Ma=0.1, 0.2 and 0.3) and viscosity (ν=η=10^{-3}, 10^{-4} and 10^{-5}).

The optimization starts by evaluating the 1% wavenumbers for d'Humières scheme, shown in Table 2, to define the wavenumber from which we hope to increase dissipation (and defines our objective function). Once determined, the optimal values of s_{10-12} and s_{13-15} are found by a brute force approach where the parametric space of the free parameters is discretized with $\Delta s_i = 0.01$ (i.e. a tolerance of 1%). Note that only values of the relaxation times in the range $[0, 2[$ are considered. For each parameter combination (Ma, ν, s_i) the shear dissipation values above the k-1% dispersion-error wavenumber is obtained. Table 1 shows the optimal values of these parameters (the combination that maximizes the shear dissipation above the k-1%). These values are very different from the free parameters proposed by d'Humières [49] where $s_{10-12} = 1.98$ and $s_{13-15} = 1.98$.

It was previously stated that the group of parameters s_{16-18} does not affect

	Ma $= 0.1$		Ma $= 0.2$		Ma $= 0.3$	
$\nu = \eta$	s_{10-12}	s_{13-15}	s_{10-12}	s_{13-15}	s_{10-12}	s_{13-15}
10^{-3}	0.62	0.81	0.92	1.12	1.11	1.32
10^{-4}	0.61	0.80	0.90	1.10	1.10	1.30
10^{-5}	0.61	0.80	0.90	1.10	1.10	1.30

Table 1: Optimized values for $s_{10} = s_{11} = s_{12}$ and $s_{13} = s_{14} = s_{15}$ at different viscosities and Mach numbers.

the shear dissipation mode, and therefore was kept constant ($s_{16-18} = 1.4$) in the optimization process. In the D3Q19, the first, s_{10-12}, and second, s_{13-15} groups of parameters relax the third order moments, while the last group, s_{16-18}, relaxes the 4th order moments. The relaxation of the 4th order moments affects the energy equation of the compressible Navier-Stokes equations, therefore we do not expect the relaxation times s_{16-18} to have a big impact in the dissipation of the shear mode. This behaviour was already reported in our previous work [1], for the D2Q9 scheme.

To confirm this, we compute the shear mode dissipation surface for the different relaxation times. Figure 3 shows the evolution of the shear mode dissipation when s_{16-18} and s_{10-12} are modified, while the rest of the relaxation parameters remain fixed. As can be seen, the last group of parameters, s_{16-18}, does not affect the shear mode dissipation. Note that the maximum dissipation corresponds to the optimized value ($s_{10-12} = 0.9$) for Ma=0.2 and $\nu = 10^{-4}$.

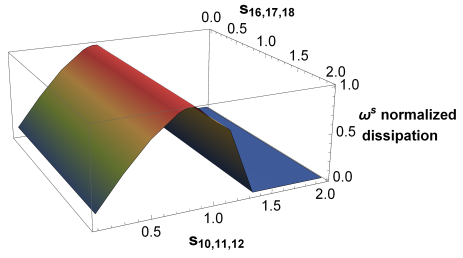

Figure 3: Shear mode dissipation surface for the different relaxation times.

Finally, Table 2 summarizes the k-1% error for d'Humières and our optimized

parameters for Mach numbers $0.1 \leq Ma \leq 0.3$ and viscosities $10^{-5} \leq \nu \leq 10^{-3}$. Our optimized values provide a slight increase in the wavenumber associated to the 1% dispersion-error, which suggests an increase in dissipation after the k-1%, and a reduction of overall dispersion error. Additionally, since our optimization ensures that the dissipation is maximized for wavenumbers above the k-1%, we can also ensure that above this threshold numerical dissipation will damp dispersive errors.

		D'Humières MRT-CM			Optimized MRT-CM		
Mode	$\nu = \eta$	Ma $= 0.1$	Ma $= 0.2$	Ma $= 0.3$	Ma $= 0.1$	Ma $= 0.2$	Ma $= 0.3$
ω^s	10^{-3}	1.141	1.225	1.382	1.162	1.350	1.414
	10^{-4}	1.141	1.224	1.382	1.162	1.330	1.393
	10^{-5}	1.141	1.224	1.382	1.162	1.330	1.393

Table 2: D3Q19 k for the 1% dispersion error between numerical and theoretical shear mode in dispersion of the physical modes.

To illustrate the effect of the optimization, the numerical shear and acoustics modes of the optimized MRT-CM are compared with d'Humières' MRT-CM, in Figure 4. These modes are computed for Ma$= 0.2$, $\nu = 10^{-3}\frac{kg}{ms}$ and $\eta = 6.7 \cdot 10^{-4}\frac{kg}{ms}$. The values of the Mach number, Ma , viscosities, ν and η, and wavenumbers, k, have been taken from [1] to permit a comparison of the results. It can be seen that the optimized MRT-CM presents a higher dissipation rate at high wavenumbers than d'Humières MRT-CM. This should result in an enhanced robustness for under-resolved simulations. Besides, it should be noticed that this increase in the dissipation rate does not affect the dispersion error at low wavenumbers. As a result, similar behaviour of the optimized MRT-CM and d'Humières MRT-CM is expected for low wavenumbers. Both approaches will be tested for an isotropic turbulent flow in the following section.

The above results allow to find a relative wavenumber threshold for the turbulent simulations to come. We relate the mesh cut-off wavelength (based on Nyquist criterion): $k_{cut-off} = \pi/2 = 1.570$, to the k-1% our optimized scheme for low Mach: $k_{1\%opt} = 1.162$, which leads to a generalized reference

value $k_{1\%opt} = 0.74k_{cut-off}$. This value will be included in the analyses of Taylor-Green vortex problem, to show that our scheme provides different (from d'Humières' MRT-CM), more accurate spectra, only above the $k_{1\%opt}$, leaving spectra for low wavenumbers unchanged.

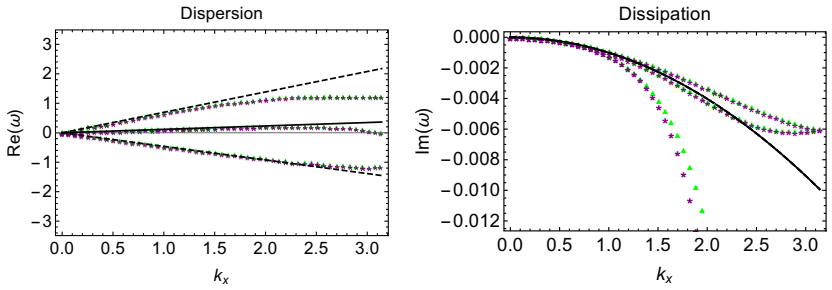

(a) (b)

Figure 4: Dispersion (a) and dissipation (b) for D3Q19 with d'Humières' MRT-CM: ▲, optimized MRT-CM: $*$ and theoretical modes (shear mode: ▬ and acoustic modes: ▪ ▪) at Ma $= 0.2$ with $\nu = 10^{-3}\frac{kg}{ms}$ (Note that the dissipation theoretical modes are overlapped).

To provide a wider context, in Appendix B we include a comparison between the numerical modes of the BGK, MRT-RM and MRT-CM D3Q19 lattice schemes. In addition, some insight on the effect of the relaxation parameters on numerical modes is given in Appendix C where d'Humières [49] and Lallemand's [18] relaxation times are compared for D3Q19 lattice scheme.

A final remark, in this work we use a von Neumann stability analysis to optimize the values of the high order relaxation parameters; therefore the effect of boundary conditions is not taken into account. It is well known that wall boundaries are important sources of numerical instabilities in LB schemes (e.g., Luo et al. [50]), so these values might change if different boundary conditions are considered. Additional work is required to study the effect of boundary conditions in the optimized values of the high order free relaxation parameters.

3. Numerical validation

In this section the new optimized scheme is compared with previous approaches found in the literature. The aim of this section is to show that the proposed scheme provides increased stability without penalizing the accuracy.

In order to study the effect of the present optimized MRT-CM on a three-dimensional turbulent configuration, the decaying Taylor-Green vortex (TGV) [36] has been simulated. It is a fundamental test case used as prototype for vortex stretching and production of small-scale eddies and therefore allows the study of the dynamics of transition to turbulence. This test-case has been widely used to study the dissipation errors of numerical schemes [37]. In the LB context, the three-dimensional TGV problem has been used to validate different LB approaches in terms of turbulence dissipation [39, 40].

In this work, the TGV is simulated with BGK, d'Humières' MRT-CM and optimized MRT-CM with different lattice resolutions. Grid resolution of $N = 32, 64, 128$ and 256 have been computed, but the analysis has focused in the under-resolved resolutions ($N = 32$ and 64), to prove if the new optimized approach provides a correct dissipation evolution.

3.1. Simulation setup

The TGV problem can be run using a variety of flow and initial conditions. The conditions and post processing used here were specified by the organizers of the AIAA First International Workshop on High-Order Methods in Computational Fluid Dynamics [37].

The domain simulated consists of a cube with length defined as $-\pi L < x, y, z < \pi L$. The boundary conditions are periodic and the initial conditions of the simulation are selected as:

$$\begin{aligned} \mathrm{u}_x =& U_0 \sin[x/L] \cos[y/L] \cos[z/L], \\ \mathrm{u}_y =& -U_0 \cos[x/L] \sin[y/L] \cos[z/L], \\ \mathrm{u}_z =& 0, \\ p =& p_0 + \frac{\rho_0 U_0^2}{16} (\cos[2x/L] + \cos[2y/L])(\cos[2z/L] + 2), \end{aligned} \tag{12}$$

where the reference density and length, ρ_0 and L, are set to one. The equation of state used is $p = c_s^2 \rho$, therefore the reference pressure is $p_0 = 1/3$.

The reference velocity, U_0, is selected through the Mach number, Ma $= U_0/c_s = 0.1$. The kinematic shear viscosity is set through the relation with the Reynolds number, Re $= U_0 L/\nu = 1600$. The physical time computed in each simulation is $t = 20t_c$, where the characteristic time, t_c, is defined as $t_c = L/U_0$. Besides, different lattice numbers ($N = 32, 64$, 128 and 256) have been used in order to test the different collision operators.

3.2. Results

To analyze the capabilities of each collision operator the dynamics of a three-dimensional decaying vortex has been computed and compared with a DNS simulation performed with a spectral method [37]. In the following, the dissipation rate and the spectrum of the kinetic energy is scrutinized for various under-resolved grids.

3.2.1. Reference results

The TGV evolution is characterized by three main steps visible in the time trace of kinetic energy dissipation rate, ε (see Eq. 13). First, the initial laminar state is transitioning to turbulence until the stretched vortex tubes break down into small scales around $t/t_c = 5$. Then the dissipation rate rises to a sharp peak near $t/t_c = 9$ corresponding to the fully turbulent state which is then decaying similarly to an isotropic and homogeneous turbulence. Figure 5 shows the different steps described through the time evolution of the kinetic energy dissipation rate, ε, for Re $= 1600$ and Ma $= 0.1$. Flow structures are represented by isosurface of the Q-criterion colored by kinetic energy. The simulation on a $N = 256$ grid is in very good agreement with the spectral results also plotted in Figure 5.

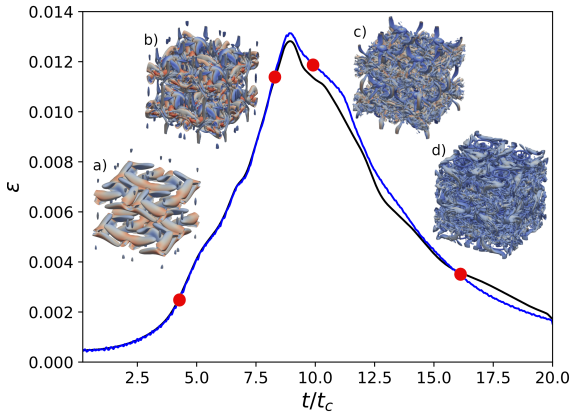

Figure 5: Isosurface of the Q-criterion colored by kinetic energy at time $t/t_c = 4$ (a), 8 (b), 10 (c), 16 (d) for Re $= 1600$ on a $N = 256$ grid ( ) compared with DNS results with $N = 512$ ( ) [37].

3.2.2. Kinetic energy dissipation rate

As illustrated before, in order to study the evolution of the fluid, the temporal evolution of the kinetic energy dissipation rate ε is calculated:

$$\varepsilon = -\frac{dE_k}{dt}. \tag{13}$$

As shown by Eq. 13, the kinetic energy dissipation rate is the temporal derivative of the kinetic energy, E_k, which is estimated using the following formula:

$$E_k = \frac{1}{\rho_0 V}\int_V \rho \frac{\mathbf{u}\cdot\mathbf{u}}{2} dV, \tag{14}$$

where the density is $\rho = \rho_0$ and V is the volume of the domain.

The results obtained with this definition are compared to the kinetic energy dissipation rate of the reference [37]. Figure 6 shows the time evolution of the kinetic energy dissipation rate, ε, for BGK and MRT-CM (with d'Humières' and optimized parameters) at different grid resolutions, taking as reference data the spectral DNS solution $N = 512$.

Analyzing the BGK behavior, the $N = 32$ and 64 simulations give rise to numerical instability at different times, while the $N = 128$ grid is stable. The $N = 32$ becomes unstable almost at the beginning of the simulation. The $N = 64$ grid simulation collapses earlier around $t/t_c = 5$, when the stretched vortex tubes break down into small scales. However, the $N = 128$ grid gives satisfactory results for the transition region and the peak but the decaying phase is not properly captured.

Regarding the MRT-CM, both sets of relaxation times are stable with the $N = 32$ and 64 grids. The laminar stage (from $t/t_c = 0$ to $t/t_c = 5$) is well predicted but the difference comes when turbulence structures starts to develop. For the coarser grid, $N = 32$, the transition evolution is faster than the spectral solution, in consequence the peak is reached earlier. Note that with the optimized values, turbulence levels are well predicted. Additionally, d'Humières' parameters have a lower dissipation rate, showing zero dissipation at the end of the simulation $t/t_c = 20$. Using $N = 64$, the dissipation rate is more accurate in the transition since the peak is produced at $t/t_c = 8$ instead $t/t_c = 9$. Then, similar behavior is produced, as in $N = 32$, where the optimized approach has some extra dissipation and ends with the correct dissipation level. Again, d'Humières' approach ends with zero dissipation rate. Finally, with the resolutions $N = 128$ and $N = 256$, both sets of parameters reproduce with a good accuracy the dynamics of transition to turbulence. Note that for $N = 256$ the results of the three approaches are overlapped.

3.2.3. Kinetic Energy spectra

The transfer of energy from large scales to small scales is referred to as inviscid energy cascade (as proposed by Kolmogorov in 1941 [51]). The largest eddies contain most of the kinetic energy, whereas the smallest eddies are responsible for the viscous dissipation of kinetic energy.

Therefore, since turbulence encompasses a wide range of eddy sizes, it is convenient to Fourier transform the velocity field to analyse the Fourier components for different wavenumbers. The components of the velocity in Fourier

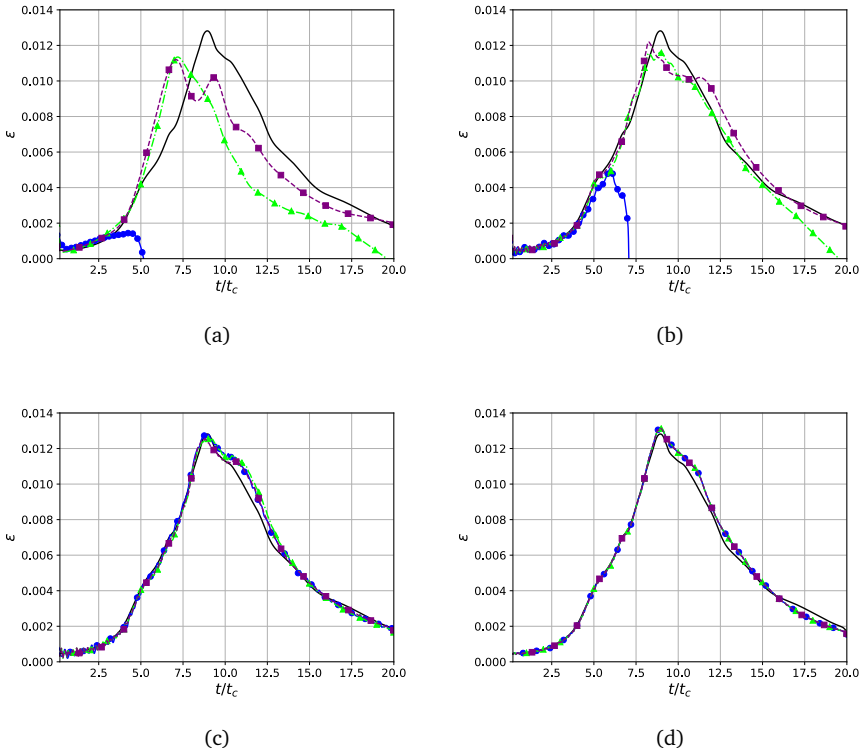

Figure 6: Kinetic energy dissipation rate for spectral DNS: ▬ on a grid $N = 512$ and BGK: ●, d'Humières' MRT-CM: ▲, and optimized MRT-CM: ■, on a grid $N = 32$ (a), $N = 64$ (b), $N = 128$ (c) and $N = 256$ (d) at $\mathrm{Re} = 1600$ and $\mathrm{Ma} = 0.1$.

space will be computed as:

$$\hat{\mathbf{u}}(||\mathbf{k}||) = \int_{\mathbb{R}^3} \mathbf{u}(\mathbf{x})\, e^{-2\pi i \mathbf{x}\cdot\mathbf{k}} d\mathbf{x}. \tag{15}$$

Subsequently, the energy spectrum function, $E(||\mathbf{k}||)$, which represents the contribution to the turbulent kinetic energy over the surfaces of spheres $S(||\mathbf{k}||)$ with radius $||\mathbf{k}|| = \sqrt{k_x^2 + k_y^2 + k_z^2}$, can be computed as:

$$E(||\mathbf{k}||) = \frac{1}{2} \oint \hat{\mathbf{u}}(\mathbf{k}) \cdot \hat{\mathbf{u}}(\mathbf{k}) dS(||\mathbf{k}||). \tag{16}$$

Continuing with the analysis, in order to understand how the optimiza-

tion affects the turbulence dissipation at the different wavenumbers, Figures 7 and 8 show the kinetic energy spectra of the optimized parameters compared with d'Humières' parameters at different grids (N= 32, 64, 128 and 256) and time steps ($t/t_c = 6, 8, 14$ and 20). The Kolmogorov law in spectral form, $E(k) \sim k^{-\frac{5}{3}}$, and the cut-off wavenumber, $k_{cut-off}$, are used for the comparison. The cut-off wavenumber, $k_{cut-off}$, is the maximum wavenumber for resolved length scales. In particular for the TGV, where $\Delta x = \frac{L}{N} = \frac{2\Pi}{N}$, the cut-off wavenumber, assuming a minimum wavelenght of $2\Delta x$ by Nyquist criterion, is $k_{cut-off} = \frac{2\pi}{2\Delta x} = \frac{\pi}{2\pi/N} = \frac{N}{2}$.

First, notice how the differences between both sets of parameters decrease when the grid resolution increases. Again, with the resolutions $N = 128$ and $N = 256$, both sets of parameters reproduce with a good accuracy the dynamics of transition to turbulence. Note that for $N = 256$ the results of the two approaches are overlapped.

Then, with $N = 32$ and 64 at $t/t_c = 6$ and 8, before and after the dissipation peak (see Figure 6) the optimized values are slightly less dissipative enabling higher wavenumbers (smaller eddies). However, differences appear at high wavenumbers for $t/t_c = 14$ and 20. We observe that the curves bifurcate after the $k_{1\%opt}$ in all cases. Let us remind the reader that these values approximate the wavenumber at which our scheme differs from d'Humières and adds dissipations for badly resolved waves. Our optimized scheme damps the extra energy build up that appear at high wavenumbers when using d'Humières' scheme, and allows us to obtain energy slopes that are close to the theoretical value of $k^{-5/3}$ as shown in Table 3. These numerical slopes, m_n are computed at $t/t_c = 20$ in the wavenumber range: $k_{EI} < k < k_{cut-off}$, where k_{EI} is the demarcation wavenumber between the energy and inertial range [52]. Both schemes are compared with the theoretical slope value, $m_t = -5/3 \approx 1.667$.

It may be concluded that our scheme is indeed useful for under-resolved simulations as it prevents energy build up and enables to retrieve the correct cascade of energy and underlying turbulent physics.

	D'Humières MRT-CM		Optimized MRT-CM	
N	m_n	$\varepsilon\%$	m_n	$\varepsilon\%$
32	-0.548	-67	-1.945	17
64	-0.436	-74	-1.867	12
128	-1.766	6	-1.740	4
256	-1.702	2	-1.695	2

Table 3: Numerical slope, m_n, and relative error, $\varepsilon = \frac{m_n - m_t}{m_t} \cdot 100$, of the kinetic energy spectra computed for wavenumber range: $k_{EI} < k < k_{cut-off}$ at $t/t_c = 20$.

Finally, our criterion for designing a scheme suitable for LES is not based on physical arguments but rather on numerical aspects. Our approach is based on obtaining the best results with the limited resources available rather than trying to simulate turbulence up to a certain percentage from the Kolmogorov length scale. In fact in the TGV simulations the Kolmogorov length scale, approximated as $l_{Kol} = L_x/Re^{3/4} = 0.012$, corresponds to a wavenumber $k_{Kol} = 2\pi/l_{Kol} = 253$ which is far from our wavenumber cut-off in all cases. Despite this, the simulations still resolve a relatively large inertial range.

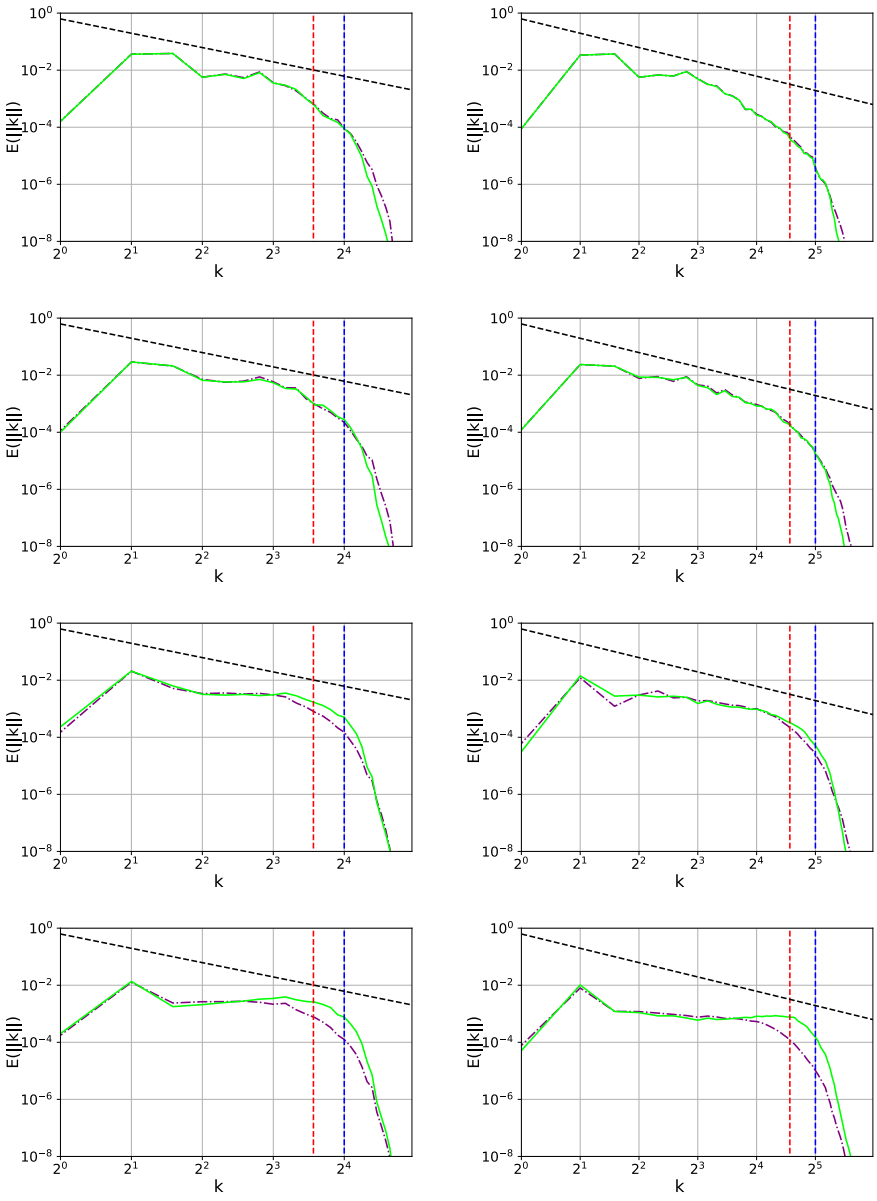

Figure 7: Kinetic energy spectra for d'Humières' MRT-CM: ▬, and optimized MRT-CM: ▬ on a $N = 32$ (left) and $N = 64$ (right) grid at $t/t_c = 6, 8, 14, 20$ (from top to bottom); Re $= 1600$ and Ma $= 0.1$ ($k^{-5/3}$: ▬, $k_{1\%opt}$: ▬ and $k_{cut-off}$: ▬).

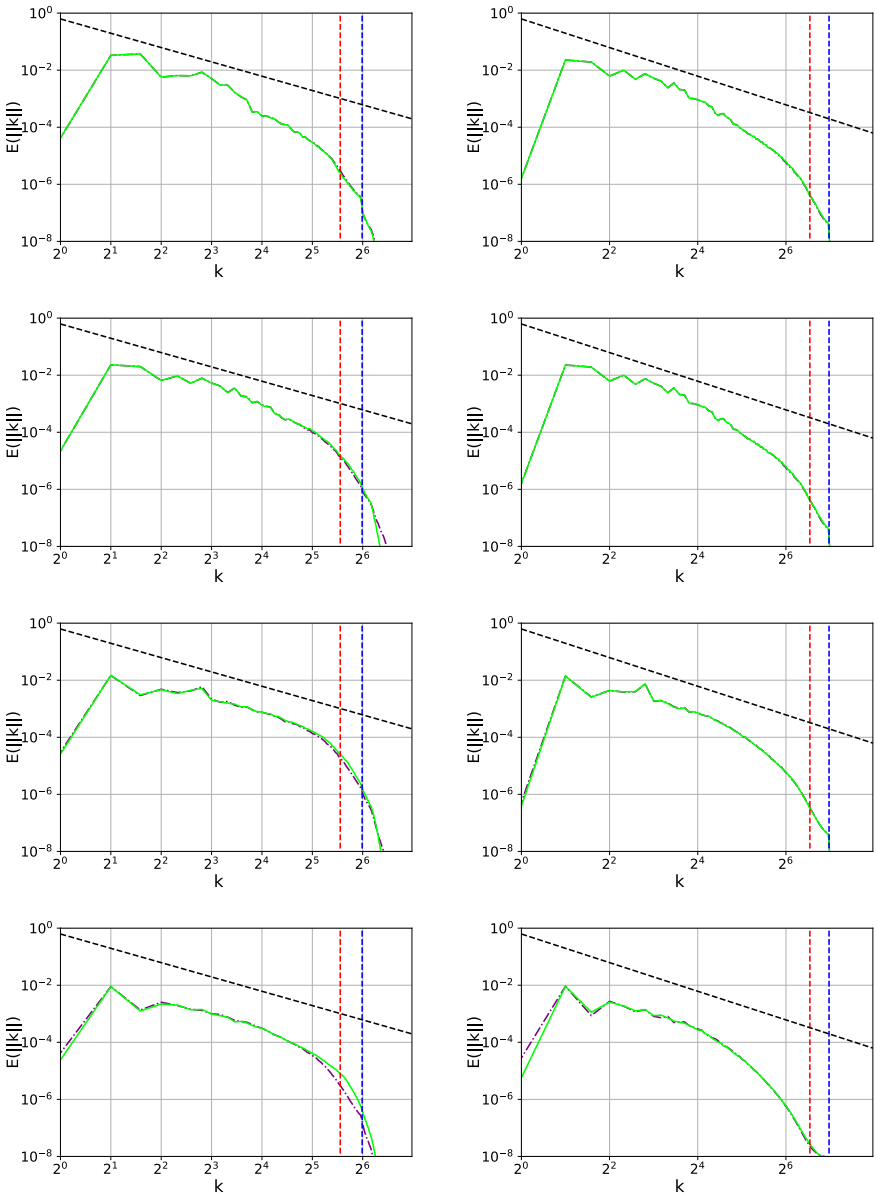

Figure 8: Kinetic energy spectra for d'Humières' MRT-CM: ▬, and optimized MRT-CM: ▬ on a $N = 128$ (left) and $N = 256$ (right) grid at $t/t_c = 6, 8, 14, 20$ (from top to bottom); Re $= 1600$ and Ma $= 0.1$ ($k^{-5/3}$: ▬, $k_{1\%opt}$: ▬ and $k_{cut-off}$: ▬).

4. Conclusions

In this paper, the free parameter (relaxation times) of the D3Q19 MRT-CM are optimized to enhance robustness for under-resolved simulations. The optimization strategy aims at maximizing the dissipation of the numerical scheme for under-resolved flow features. The limit between well- and under-resolved waves is based on von Neumann linear stability analyses and the so called k-1% dispersion-error rule. The D3Q19 optimized MRT-CM scheme is compared with standard BGK and MRT-CM schemes by means of the Taylor-Green vortex turbulent test. The three schemes perform similarly for well-resolved setups, however the optimized MRT-CM provides significantly better results than BGK and MRT-CM for under-resolved flow conditions. In particular, the optimized MRT-CM is more accurate at capturing the three-dimensional kinetic energy evolution and energy cascade for under-resolved simulations; providing the bases for more general Large Eddy Simulation models.

Acknowledgment

This project has received funding from the European Unionś Horizon 2020 research and innovation programme under grant agreement No 785549 (Fire-Extintion: H2020-CS2-CFP06-2017-01).

The authors acknowledge the computer resources and technical assistance provided by the Centro de Supercomputación y Visualización de Madrid (CeSViMa).

Appendix A. Moments matrix for D3Q19

Based on Dubois et al. [45], the following set of moments are proposed:

$$\begin{aligned} X^m Y^l Z^k =& (X^0 Y^0, X, Y, Z, XY, XZ, YZ, X^2 - Y^2, X^2 - Z^2, X^2 + Y^2 + Z^2, \\ & XY^2 + XZ^2, X^2 Y + YZ^2, X^2 Z + Y^2 Z, XY^2 - XZ^2, X^2 Y - YZ^2, X^2 Z - Y^2 Z, \\ & X^2 Y^2 + X^2 Z^2 + Y^2 Z^2, X^2 Y^2 + X^2 Z^2 - Y^2 Z^2, X^2 Y^2 - X^2 Z^2)^T; m, l, k = 0, 1, 2 \end{aligned} \tag{A.1}$$

Applying the Gram-Schmidt orthogonalization procedure to Eq. A.1, the matrix $M(\mathbf{u})$ is obtained:

$$M(\mathbf{u}) = \begin{pmatrix} X^0 Y^0 Z^0 \\ X \\ Y \\ Z \\ XY \\ XZ \\ YZ \\ X^2 - Y^2 \\ (X^2 + Y^2 + Z^2) - 3Z^2 \\ (X^2 + Y^2 + Z^2) - 2 \\ 3(XY^2 + XZ^2) - 4X \\ 3(YX^2 + YZ^2) - 4Y \\ 3(ZX^2 + ZY^2) - 4Z \\ (XY^2 - XZ^2) \\ (YX^2 - YZ^2) \\ (ZX^2 - ZY^2) \\ 3(X^2Y^2 + X^2Z^2 - 2Y^2Z^2) - (2(2X^2 - Y^2 - Z^2)) \\ 3(X^2Y^2 - X^2Z^2) - 2(Y^2 - Z^2) \\ 3(X^2Y^2 + X^2Z^2 + Y^2Z^2) - 4(X^2 + Y^2 + Z^2) + 4 \end{pmatrix} = \begin{pmatrix} \rho \mid_i \\ j_x \mid_i \\ j_y \mid_i \\ j_z \mid_i \\ p_{xy} \mid_i \\ p_{xz} \mid_i \\ p_{yz} \mid_i \\ p_{ww} \mid_i \\ 3p_{xx} \mid_i \\ e \mid_i \\ q_x \mid_i \\ q_y \mid_i \\ q_z \mid_i \\ m_x \mid_i \\ m_y \mid_i \\ m_z \mid_i \\ 3\pi_{xx} \mid_i \\ \pi_{ww} \mid_i \\ \epsilon \mid_i \end{pmatrix} \tag{A.2}$$

As can be seen, the selection of moments has a physical foundation. ρ is the density, e is the kinetic energy, ϵ is related to the kinetic energy square, $\mathbf{j} = \rho\mathbf{u}$ components correspond to components of momentum, $\mathbf{q}$ components correspond to the internal energy components, $\mathbf{p}$ components correspond to the

symmetric traceless viscous stress tensor, π is related with the kinetic energy and the viscous stress tensor and m components are the asymmetric third-order moments.

Hence the transformation matrix in raw moments is $M(\mathbf{u}=\mathbf{0})$ with $X = e_x$, $Y = e_y$ and $Z = e_z$.

$$M(\mathbf{0}) = \begin{pmatrix}
1 & 1 & 1 & 1 & 1 & 1 & 1 & 1 & 1 & 1 & 1 & 1 & 1 & 1 & 1 & 1 & 1 & 1 & 1 \\
0 & -1 & 0 & 0 & -1 & -1 & -1 & -1 & 0 & 0 & 1 & 0 & 0 & 1 & 1 & 1 & 1 & 0 & 0 \\
0 & 0 & -1 & 0 & -1 & 1 & 0 & 0 & -1 & -1 & 0 & 1 & 0 & 1 & -1 & 0 & 0 & 1 & 1 \\
0 & 0 & 0 & -1 & 0 & 0 & -1 & 1 & -1 & 1 & 0 & 0 & 1 & 0 & 0 & 1 & -1 & 1 & -1 \\
0 & 0 & 0 & 0 & 1 & -1 & 0 & 0 & 0 & 0 & 0 & 0 & 0 & 1 & -1 & 0 & 0 & 0 & 0 \\
0 & 0 & 0 & 0 & 0 & 0 & 1 & -1 & 0 & 0 & 0 & 0 & 0 & 0 & 0 & 1 & -1 & 0 & 0 \\
0 & 0 & 0 & 0 & 0 & 0 & 0 & 0 & 1 & -1 & 0 & 0 & 0 & 0 & 0 & 0 & 0 & 1 & -1 \\
0 & 1 & -1 & 0 & 0 & 0 & 1 & 1 & -1 & -1 & 1 & -1 & 0 & 0 & 0 & 1 & 1 & -1 & -1 \\
0 & 1 & 1 & -2 & 2 & 2 & -1 & -1 & -1 & -1 & 1 & 1 & -2 & 2 & 2 & -1 & -1 & -1 & -1 \\
-2 & -1 & -1 & -1 & 0 & 0 & 0 & 0 & 0 & 0 & -1 & -1 & -1 & 0 & 0 & 0 & 0 & 0 & 0 \\
0 & 4 & 0 & 0 & 1 & 1 & 1 & 1 & 0 & 0 & -4 & 0 & 0 & -1 & -1 & -1 & -1 & 0 & 0 \\
0 & 0 & 4 & 0 & 1 & -1 & 0 & 0 & 1 & 1 & 0 & -4 & 0 & -1 & 1 & 0 & 0 & -1 & -1 \\
0 & 0 & 0 & 4 & 0 & 0 & 1 & -1 & 1 & -1 & 0 & 0 & -4 & 0 & 0 & -1 & 1 & -1 & 1 \\
0 & 0 & 0 & 0 & -1 & -1 & 1 & 1 & 0 & 0 & 0 & 0 & 0 & 1 & 1 & -1 & -1 & 0 & 0 \\
0 & 0 & 0 & 0 & -1 & 1 & 0 & 0 & 1 & 1 & 0 & 0 & 0 & 1 & -1 & 0 & 0 & -1 & -1 \\
0 & 0 & 0 & 0 & 0 & 0 & -1 & 1 & 1 & -1 & 0 & 0 & 0 & 0 & 0 & 1 & -1 & -1 & 1 \\
0 & -4 & 2 & 2 & 1 & 1 & 1 & 1 & -2 & -2 & -4 & 2 & 2 & 1 & 1 & 1 & 1 & -2 & -2 \\
0 & 0 & -2 & 2 & 1 & 1 & -1 & -1 & 0 & 0 & 0 & -2 & 2 & 1 & 1 & -1 & -1 & 0 & 0 \\
4 & 0 & 0 & 0 & -1 & -1 & -1 & -1 & -1 & -1 & 0 & 0 & 0 & -1 & -1 & -1 & -1 & -1 & -1
\end{pmatrix} \tag{A.3}$$

Finally, as it was explained before, S_{kl} is a diagonal matrix. The entries of this diagonal matrix account for the relaxation times, s_i, of the different moments. In particular, in the D3Q19 scheme this reads:

$$S_{kk} = (s_0, s_1, s_2, s_3, s_4, s_5, s_6, s_7, s_8, s_9, s_{10}, s_{11}, s_{12}, s_{13}, s_{14}, s_{15}, s_{16}, s_{17}, s_{18}). \tag{A.4}$$

In the case of the MRT collision model, the hydrodynamic quantities (density and momentum) can be imposed with any value of s_0, s_1, s_2 and s_3, provided $\rho = \rho^{eq}$ and $\mathbf{u} = \mathbf{u}^{eq}$. These are set to zero.

Commonly in the literature, the rest of the relaxation times are set as in d'Humières' [49]. D'Humières' diagonal parameters in the collision matrix of

the MRT collision operators reads:

$$S_{ii} = (0, 0, 0, 0, s_4, s_5, s_6, s_7, s_8, s_9, 1.2, 1.2, 1.2, 1.98, 1.98, 1.98, 1.4, 1.4, 1.4). \tag{A.5}$$

As for the BGK collision operator, the Chapman-Enskog expansion establishes the relation between the relaxation times and the kinematic shear and bulk viscosities of the macroscopic fluid [18]. In the MRT approach the kinematic viscosity, ν, and the bulk viscosity, η, are related to the relaxations parameters (s_4, s_5, s_6, s_7, s_8, s_9) associated to the second order moments. As a result, this approach removes some of the constraints of the BGK collision operator. In particular, the viscosities read:

$$\nu = c_s^2(\frac{1}{s_i} - \frac{\Delta t}{2}) \text{ with } i = 4, \ldots, 8 \ , \ \eta = \frac{2}{D} c_s^2(\frac{1}{s_9} - \frac{\Delta t}{2}). \tag{A.6}$$

It is important to notice that, having identified the relations between the kinematic and bulk viscosities with the relaxation times, the higher order moments relaxation times, s_{10-18}, remain free parameters. Finally, it should be mentioned that the relaxation values, s_i, related with the viscosities must lie between 0 and 2 since the kinematic and bulk viscosity cannot be negative (see Eq. A.6 with $\Delta t = 1$).

Appendix B. BGK, MRT-RM and MRT-CM collision operators

In this appendix, the numerical modes of three different collision operators (BGK, MRT-RM and MRT-CM) are compared. Following our previous work [1] regarding an optimization of the D2Q9 MRT-CM, the bulk viscosity is fixed in BGK and MRT approaches to the same value to permit the comparison between both approaches. So, the relation $\eta^{\text{BGK}} = \frac{2}{3}\nu$ is also applied to the MRT collision operator. In particular, the kinematic viscosity is fixed to $10^{-3}\frac{kg}{ms}$ and consequently the bulk viscosity is fixed to $6.7 \cdot 10^{-4}\frac{kg}{ms}$. That means a value of $\tau = 0.503$ for the BGK collision operator and values $s_{4-9} = 1.988$ for the MRT

collision operators. The rest of relaxation times are fixed to the values proposed by d'Humières et al. [49] (see Eq. A.5).

Figure B.9 shows the dispersion and dissipation of the three approaches compared with the theoretical modes for Ma$= 0.2$. Notice that the dispersion errors in Figure 9(a) at low wavenumbers is negligible for the kinetic modes. But for large wavenumbers we observe the development of non-negligible dispersion errors, which should be dissipated correctly.

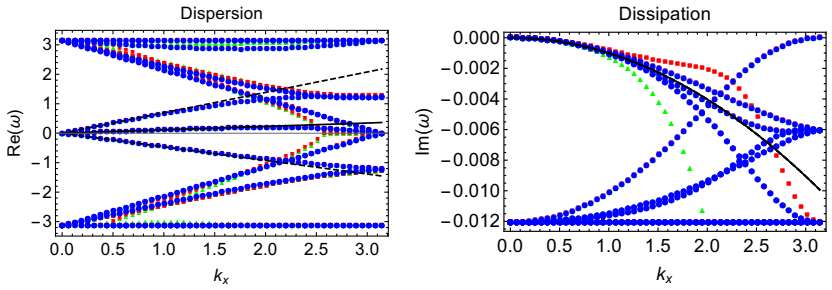

(a) (b)

Figure B.9: Dispersion (a) and dissipation (b) for D3Q19 with BGK: ●, d'Humières' MRT-RM: ■, d'Humières' MRT-CM: ▲ and theoretical modes (shear mode: ━, and acoustic modes: ▬) at Ma $= 0.2$ with $\nu = 10^{-3}\,\frac{kg}{ms}$ (Note that the dissipation theoretical modes are overlapped).

Figure 9(b) shows dissipation where the theoretical modes (shear and acoustic) overlap, which is due the contribution of the kinematic and bulk viscosities in Eq. 8. Also as expected, the modes have a similar behaviour as in D2Q9 [1] regarding the dissipation of the shear mode. The MRT-CM approaches presents a higher dissipation rate at high wavenumbers.

Besides, the MRT-RM seems more unstable compared with the D2Q9 lattice scheme at the same fluid conditions (see Figure 3(b) in [1]). These differences between D2Q9 and D3Q19 lattice schemes could come from the different values used from the literature for the free parameters, Lallemand's [18] and d'Humières' [49] values for D2Q9 and D3Q19 respectively. This assumption is clarified in the Appendix C.

Appendix C. Comparison between Lallemand's and d'Humières' parameters:

As mentioned before, initially Lallemand and Luo [18] proposed values for the free parameters of the MRT collision operator for the D2Q9 lattice scheme. Later, d'Humières' [49] suggested different values for the D3Q19 MRT relaxation times. Both sets of parameters were obtained through an optimization process based on linear stability analysis.

In this section, both Lallemand's and d'Humières' parameters are compared for the D3Q19. So, taking into account the geometrical relation between the D2Q9 and D3Q19 lattice schemes, the Lallemand's parameters for the D3Q19 discretization are:

$$S_{ii} = (0, 0, 0, 0, s_4, s_5, s_6, s_7, s_8, s_9, 1.9, 1.9, 1.9, 1.9, 1.9, 1.9, 1.54, 1.54, 1.54). \tag{C.1}$$

Figure C.10 shows the dispersion and dissipation for D3Q19 with Lallemand's parameters with $\nu = 10^{-3}\frac{kg}{ms}$ and $\eta = 6.7 \cdot 10^{-4}\frac{kg}{ms}$ $(s_{4-9} = 1.9988)$ at Ma $= 0.2$. Notice how the shear mode dissipation is identical compared with the D2Q9 lattice scheme (see Figure 3(b) in [1]), which uses the Lallemand's parameters (Eq. C.1). These plots confirm the assumption done previously.

Figure C.11 compares both Lallemand's and d'Humières' parameters for the MRT-CM collision operator. Note how the dissipation of the shear mode is higher with d'Humières', because the second order moments are related with the shear mode dissipation. In this work, d'Humières' values are used due to the higher dissipation at high wavenumbers. This will prove advantageous to dissipate under-resolved waves.

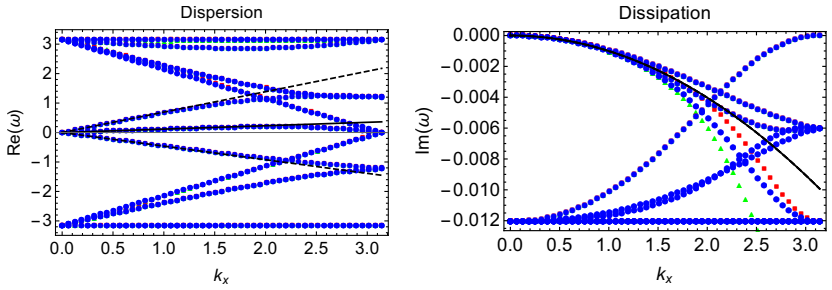

(a) (b)

Figure C.10: Dispersion (a) and dissipation (b) for with D3Q19 BGK: ●, Lallemand's MRT-RM: ■, Lallemand's MRT-CM: ▲ and theoretical modes (shear mode: ▬, and acoustic modes: ▪▪) with $\nu = 10^{-3}\frac{kg}{ms}$ and $\eta = 6.7 \cdot 10^{-4}\frac{kg}{ms}$ $(s_{4-9} = 1.9988)$ at Ma $= 0.2$ (Note that the dissipation theoretical modes are overlapped).

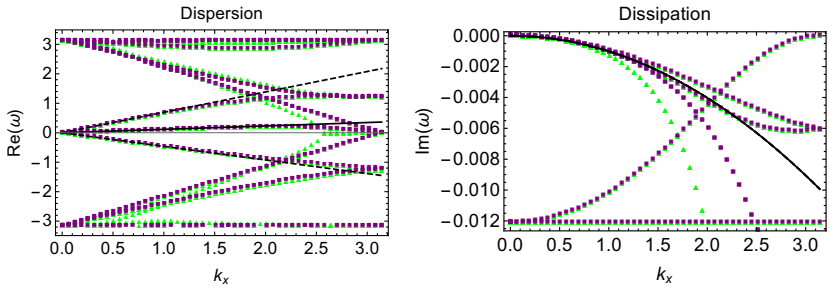

(a) (b)

Figure C.11: Dispersion (a) and dissipation (b) for D3Q19 with Lallemand's MRT-CM: (■), d'Humières' MRT-CM: (▲), and theoretical modes (shear mode, ▬, and acoustic mode, ▪▪) with $\nu = 10^{-3}\frac{kg}{ms}$ and $\eta = 6.7 \cdot 10^{-4}\frac{kg}{ms}$ $(s_{4-9} = 1.994)$ at Ma $= 0.2$ (Note that the dissipation theoretical modes are overlapped).

References

[1] M. Chávez-Modena, E. Ferrer, G. Rubio, Improving the stability of multiple-relaxation lattice boltzmann methods with central moments, Computers & Fluids 172 (2018) 397–409.

[2] S. Succi, The lattice Boltzmann equation, For Fluid Dynamics and Beyond (2001).

[3] C. C. Kiris, D. Stich, J. A. Housman, J. G. Kocheemoolayil, M. F. Barad, F. Cadieux, Application of lattice Boltzmann and Navier-Stokes methods to NASA wall mounted hump, in: 2018 Fluid Dynamics Conference, 2018, p. 3855.

[4] C. L. Rumsey, J. P. Slotnick, A. J. Sclafani, Overview and summary of the third AIAA high lift prediction workshop, Journal of Aircraft 56 (2) (2019) 621–644.

[5] M. F. Barad, J. G. Kocheemoolayil, C. C. Kiris, Lattice Boltzmann and Navier-Stokes cartesian CFD approaches for airframe noise predictions, in: 23rd AIAA Computational fluid dynamics conference, 2017, p. 4404.

[6] B. Konig, E. Fares, M. Murayama, Y. Ito, PowerFLOW simulations for the third AIAA high-lift prediction workshop, in: 2018 AIAA Aerospace Sciences Meeting, 2018, p. 1255.

[7] H. Xu, P. Sagaut, Optimal low-dispersion low-dissipation LBM schemes for computational aeroacoustics, Journal of Computational Physics 230 (13) (2011) 5353–5382.

[8] R. Brionnaud, M. Chávez-Modena, G. Trapani, D. M. Holman, Direct noise computation with a lattice-Boltzmann method and application to industrial test cases, in: 22nd AIAA/CEAS Aeroacoustics Conference, 2016, p. 2969.

[9] D. Chatterjee, S. Chakraborty, A hybrid lattice Boltzmann model for solid–liquid phase transition in presence of fluid flow, Physics Letters A 351 (4-5) (2006) 359–367.

[10] Y. Gan, A. Xu, G. Zhang, S. Succi, Discrete Boltzmann modeling of multiphase flows: hydrodynamic and thermodynamic non-equilibrium effects, Soft Matter 11 (26) (2015) 5336–5345.

[11] N. S. Martys, H. Chen, Simulation of multicomponent fluids in complex three-dimensional geometries by the lattice Boltzmann method, Physical review E 53 (1) (1996) 743.

[12] Y. H. Qian, D. D'Humières, P. Lallemand, Lattice BGK models for Navier-Stokes equation, EPL (Europhysics Letters) 17 (1992) 479.

[13] F. J. Higuera, J. Jiménez, Boltzmann approach to lattice gas simulations, EPL (Europhysics Letters) 9 (1989) 663.

[14] C. Coreixas, B. Chopard, J. Latt, Comprehensive comparison of collision models in the lattice Boltzmann framework: Theoretical investigations, arXiv preprint arXiv:1904.12948 (2019).

[15] P. L. Bhatnagar, E. P. Gross, M. Krook, A model for collision processes in gases. I. small amplitude processes in charged and neutral one-component systems, Physical review 94 (3) (1954) 511.

[16] Z. Guo, C. Zheng, T. Zhao, A lattice BGK scheme with general propagation, Journal of Scientific Computing 16 (4) (2001) 569–585.

[17] D. d'Humieres, Generalized lattice-Boltzmann equations, Progress in Astronautics and Aeronautics 159 (1994) 450–450.

[18] P. Lallemand, L.-S. Luo, Theory of the lattice Boltzmann method: Dispersion, dissipation, isotropy, galilean invariance, and stability, Physical Review E 61 (6) (2000) 6546.

[19] M. Geier, A. Greiner, J. G. Korvink, Cascaded digital lattice Boltzmann automata for high Reynolds number flow, Physical Review E 73 (6) (2006) 066705.

[20] M. Geier, A. Greiner, J. Korvink, A factorized central moment lattice Boltzmann method, The European Physical Journal Special Topics 171 (1) (2009) 55–61.

[21] K. N. Premnath, S. Banerjee, On the three-dimensional central moment lattice Boltzmann method, Journal of Statistical Physics 143 (4) (2011) 747–794.

[22] S. Adam, F. Hajabdollahi, K. Premnath, Cascaded lattice Boltzmann modeling and simulations of three-dimensional non-Newtonian fluid flows, arXiv preprint arXiv:1908.05396 (2019).

[23] J. G. Charney, R. Fjörtoft, J. v. Neumann, Numerical integration of the barotropic vorticity equation, Tellus 2 (4) (1950) 237–254.

[24] J. D. Sterling, S. Chen, Stability analysis of lattice Boltzmann methods, Journal of Computational Physics 123 (1) (1996) 196–206.

[25] D. Siebert, L. Hegele Jr, P. Philippi, Lattice Boltzmann equation linear stability analysis: thermal and athermal models, Physical Review E 77 (2) (2008) 026707.

[26] O. Malaspinas, Increasing stability and accuracy of the lattice Boltzmann scheme: recursivity and regularization, arXiv preprint arXiv:1505.06900 (2015).

[27] K. K. Mattila, P. C. Philippi, L. A. Hegele Jr, High-order regularization in lattice-Boltzmann equations, Physics of Fluids 29 (4) (2017) 046103.

[28] C. Coreixas, G. Wissocq, G. Puigt, J.-F. Boussuge, P. Sagaut, Recursive regularization step for high-order lattice Boltzmann methods, Physical Review E 96 (3) (2017) 033306.

[29] S. Marié, D. Ricot, P. Sagaut, Comparison between lattice Boltzmann method and Navier-Stokes high order schemes for computational aeroacoustics, Journal of Computational Physics 228 (4) (2009) 1056–1070.

[30] F. Dubois, T. Fevrier, B. Graille, On the stability of a relative velocity lattice Boltzmann scheme for compressible Navier-Stokes equations, Comptes Rendus Mécanique 343 (10) (2015) 599–610.

[31] G. Wissocq, P. Sagaut, J.-F. Boussuge, An extended spectral analysis of the lattice Boltzmann method: modal interactions and stability issues, Journal of Computational Physics 380 (2019) 311–333.

[32] S. Chapman, T. G. Cowling, The mathematical theory of non-uniform gases: an account of the kinetic theory of viscosity, thermal conduction and diffusion in gases, Cambridge university press, 1970.

[33] H. Xu, O. Malaspinas, P. Sagaut, Sensitivity analysis and determination of free relaxation parameters for the weakly-compressible MRT-LBM schemes, Journal of Computational Physics 231 (21) (2012) 7335–7367.

[34] Y. Ning, K. N. Premnath, D. V. Patil, Numerical study of the properties of the central moment lattice Boltzmann method, International Journal for Numerical Methods in Fluids 82 (2) (2016) 59–90.

[35] R. Moura, S. Sherwin, J. Peiró, Linear dispersion–diffusion analysis and its application to under-resolved turbulence simulations using Discontinuous Galerkin spectral/hp methods, Journal of Computational Physics 298 (2015) 695–710.

[36] G. I. Taylor, A. E. Green, Mechanism of the production of small eddies from large ones, Proc. R. Soc. Lond. A 158 (895) (1937) 499–521.

[37] Z. J. Wang, K. Fidkowski, R. Abgrall, F. Bassi, D. Caraeni, A. Cary, H. Deconinck, R. Hartmann, K. Hillewaert, H. T. Huynh, et al., High-order CFD methods: current status and perspective, International Journal for Numerical Methods in Fluids 72 (8) (2013) 811–845.

[38] J. Manzanero, E. Ferrer, G. Rubio, E. Valero, Design of a smagorinsky spectral vanishing viscosity turbulence model for discontinuous galerkin methods, Computers & Fluids (2020) 104440.

[39] I. V. Karlin, A. G. Tomboulides, C. E. Frouzakis, S. Ansumali, Kinetically reduced local Navier-Stokes equations: An alternative approach to hydrodynamics, Physical Review E 74 (3) (2006) 035702.

[40] S. Marié, X. Gloerfelt, Adaptive filtering for the lattice Boltzmann method, Journal of Computational Physics 333 (2017) 212–226.

[41] M. Haussmann, S. Simonis, H. Nirschl, M. J. Krause, Direct numerical simulation of decaying homogeneous isotropic turbulence numerical experiments on stability, consistency and accuracy of distinct lattice Boltzmann methods, International Journal of Modern Physics C (2019) 1950074.

[42] G. R. McNamara, G. Zanetti, Use of the Boltzmann equation to simulate lattice-gas automata, Physical Review Letters 61 (1988) 2332–2335.

[43] X. He, L.-S. Luo, Theory of the lattice Boltzmann method: From the Boltzmann equation to the lattice Boltzmann equation, Physical Review E 56 (6) (1997) 6811.

[44] Z. Guo, C. Shu, Lattice Boltzmann method and its applications in engineering, Vol. 3, World Scientific, 2013.

[45] F. Dubois, T. Fevrier, B. Graille, Lattice Boltzmann schemes with relative velocities, Communications in Computational Physics 17 (04) (2015) 1088–1112.

[46] L. Landau, E. Lifshitz, Fluid mechanics: Landau and Lifshitz: course of theoretical physics, Vol. 6, Elsevier, 2013.

[47] G. Gassner, D. A. Kopriva, A comparison of the dispersion and dissipation errors of Gauss and Gauss–Lobatto discontinuous Galerkin spectral

element methods, SIAM Journal on Scientific Computing 33 (5) (2011) 2560–2579.

[48] J. Manzanero, G. Rubio, E. Ferrer, E. Valero, Dispersion-diffusion analysis for advection problems with non-constant coefficients: applications to Discontinuous Galerkin formulations., SIAM Journal of Scientific Computing 40 (2) (2018) A747–A768.

[49] D. d'Humières, Multiple-relaxation-time lattice Boltzmann models in three dimensions, Philosophical Transactions of the Royal Society of London. Series A: Mathematical, Physical and Engineering Sciences 360 (1792) (2002) 437–451.

[50] L.-S. Luo, W. Liao, X. Chen, Y. Peng, W. Zhang, et al., Numerics of the lattice Boltzmann method: Effects of collision models on the lattice Boltzmann simulations, Physical Review E 83 (5) (2011) 056710.

[51] A. N. Kolmogorov, The local structure of turbulence in incompressible viscous fluid for very large Reynolds numbers, in: Dokl. Akad. Nauk SSSR, Vol. 30, 1941, pp. 299–303.

[52] S. B. Pope, Turbulent flows (2001).